Omnidirectional plane-wave destruction[a]

[a]Published in Geophysics, 78, no. 5, V171-V179, (2013)

Zhonghuan Chen[1], *Sergey Fomel*[2], *and Wenkai Lu*[1]

ABSTRACT

Steep structures in seismic data may bring directional aliasing, thus plane-wave destruction (PWD) filter can not obtain an accurate dip estimation. We propose to interpret plane-wave construction (PWC) filter as a line-interpolating operator and introduce a novel circle-interpolating model. The circle-interpolating PWC can avoid phase-wrapping problems, and the related circle-interpolating plane-wave destruction (PWD) can avoid aliasing problems. We design a 2D maxflat fractional delay filter to implement the circle interpolation, and prove that the 2D maxflat filter is separable in each direction. Using the maxflat fractional delay filter in the circle interpolation, we propose the omnidirectional plane-wave destruction (OPWD). The omnidirectional PWD can handle both vertical and horizontal structures. With a synthetic example, we show how to obtain an omnidirectional dip estimation using the proposed omnidirectional PWD. An application of the omnidirectional PWD to a field dataset improves the results of predictive painting and event picking, as compared to conventional PWD.

INTRODUCTION

Seismic wavefields can be approximated by local plane waves, and the local slope field of these plane waves has been a significant parameter in seismic analysis. Plane-wave destruction (PWD) is one of the most popular tools to estimate the slope field. The linear PWD proposed by Claerbout (1992) uses explicit finite differences and obtains the slope field by least-squares estimation. The nonlinear PWD proposed by Fomel (2002) uses the maxflat fractional delay filter (Thiran, 1971; Zhang, 2009) to approximate a linear phase operator (or phase shift operator) and to provide a polynomial equation for the local slope (Chen et al., 2013). When the nonlinear PWD is applied iteratively, its first iteration corresponds to the linear PWD.

Local slope field has been widely applied in seismic applications. In applications such as model parameterization (Fomel and Guitton, 2006; Fomel et al., 2007), trace interpolation (Bardan, 1987) and wavefield separation and denoising (Harlan et al., 1984) in prestack datasets, seismic events usually have moderate slopes. However, in other applications, there might be steep or even vertical structures in the data and the slopes might be large or even infinite. Some common examples are: (1) migrated datasets, where geological structures can be steeply dipping, and attribute analysis

may require the slope field (Marfurt et al., 1999); (2) time slices, where azimuths can follow any directions (Marfurt, 2006, Figure 2a is a good example); (3) profiles with insufficient horizontal sampling interval, causing dip aliasing problems (Barnes, 1996). Hale (2007) has shown that neither linear nor nonlinear PWD can cope with these steep structures well. In this case, the PWD-based slope estimation may be inaccurate.

In order to handle steep structures, several methods have been proposed to improve the linear PWD: Davis (1991) and Noye (2000) introduced other finite-difference methods to obtain a better phase-shift response. Hale (2007) applied the linear PWD in both horizontal and vertical directions, to construct the directional Laplacian operator. Schleicher et al. (2009) proposed total least-squares estimation to improve the least-squares estimation.

In this paper, we propose to interpret the phase shift operator in the nonlinear PWD as a 1D wavefield interpolator (vertical interpolation in a seismic trace). In order to handle omnidirectional structures, we introduce a 2D interpolator, which interpolates the wavefield along a circle instead of a vertical line. Circle interpolation can avoid aliasing problems and enable efficient modeling of steep structures.

We design a 2D maxflat fractional delay filter to implement circle interpolation. This 2D filter can be decoupled into a cascade of two 1D filters applied in different directions. Using the polynomial design of the maxflat fractional delay filter (Chen et al., 2013), we propose an omnidirectional plane-wave destruction (OPWD). We use a synthetic example to demonstrate the omnidirectional modeling ability and apply OPWD to improve events picking for a field dataset.

FROM LINE INTERPOLATION TO CIRCLE INTERPOLATION

Considering the wavefield $u(x_1, x_2)$ observed in a 2D sampling system and following Fomel (2002), plane-wave destruction can be represented in the Z-transform domain as

$$(1 - Z_2 Z_1^p) U(Z_1, Z_2) = 0 \ , \tag{1}$$

where Z_1, Z_2 are the unit shift operators in the first and second dimensions. $U(Z_1, Z_2)$ (or U for convenience) denotes the Z transform of $u(x_1, x_2)$. p is the local slope. We call $Z_2 Z_1^p$ and $1 - Z_2 Z_1^p$ plane-wave constructor and destructor, respectively. The slope p has the following relationship with the dip angle θ: $p = \tan\theta$.

Applying $Z_2 Z_1^p$ at one point, for example, point O in Figure 1, PWC obtains the wavefield at the point with a unit shift in the second dimension and p unit shifts in the first dimension, denoted by $A(x_1 + p\Delta x_1, x_2 + \Delta x_2)$. As $-\pi/2 \le \theta \le \pi/2$, p can be any value from $-\infty$ to $+\infty$. That is to say, the forward plane-wave constructor $Z_2 Z_1^p$ interpolates the wavefield along the vertical line at $x_2 + \Delta x_2$. Similarly, the backward PWC interpolates the wavefield along the vertical line at $x_2 - \Delta x_2$.

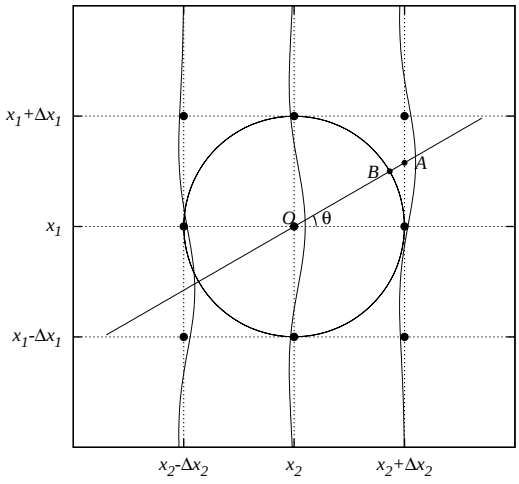

Figure 1: Interpolation in plane-wave construction: line-interpolating PWC interpolates the wavefield at point A, while circle-interpolating PWC interpolates at point B.

In order to handle both vertical and horizontal structures, we propose to modify the plane-wave destruction in equation 1 into the following form:

$$(1 - Z_2^{p_2} Z_1^{p_1})U = 0, \tag{2}$$

where p_1, p_2 are parameters related to the trial dip angle, as follows: $p_1 = r \sin\theta$, $p_2 = r \cos\theta$.

In other words, we consider a circle in polar coordinates, parameterized by the radius r and the dip angle θ. Applying the new PWC $Z_2^{p_2} Z_1^{p_1}$ at point O, it obtains the wavefield at the point with p_1 unit shifts in the first dimension and p_2 unit shifts in the second dimension. That is point $B(x_1 + p_1\Delta x_1, x_2 + p_2\Delta x_2)$. As θ changes, the new PWC $Z_1^{p_1} Z_2^{p_2}$ interpolates the wavefield along a circle with radius r. We draw the interpolating circle with $r = 1$ in Figure 1. The circle-interpolating PWC $Z_1^{p_1} Z_2^{p_2}$ corresponds to a 2D interpolation. Equation 1 can also be seen as a special case of equation 2 when $p_2 = 1$. Compared with the 1D line-interpolating method, the main benefit of circle interpolation is its antialiasing ability.

Anti-aliasing ability

We compare the line-interpolating and circle-interpolating PWD operators in the frequency domain. At different dip angles, the magnitude responses of $1 - Z_2 Z_1^p$ and $1 - Z_1^{p_1} Z_2^{p_2}$ are shown in Figure 2: When dip angle $\theta = 20°$, the two operators have similar responses (Figure 2a and 2d); when $\theta = 50°$, the line-interpolating PWD

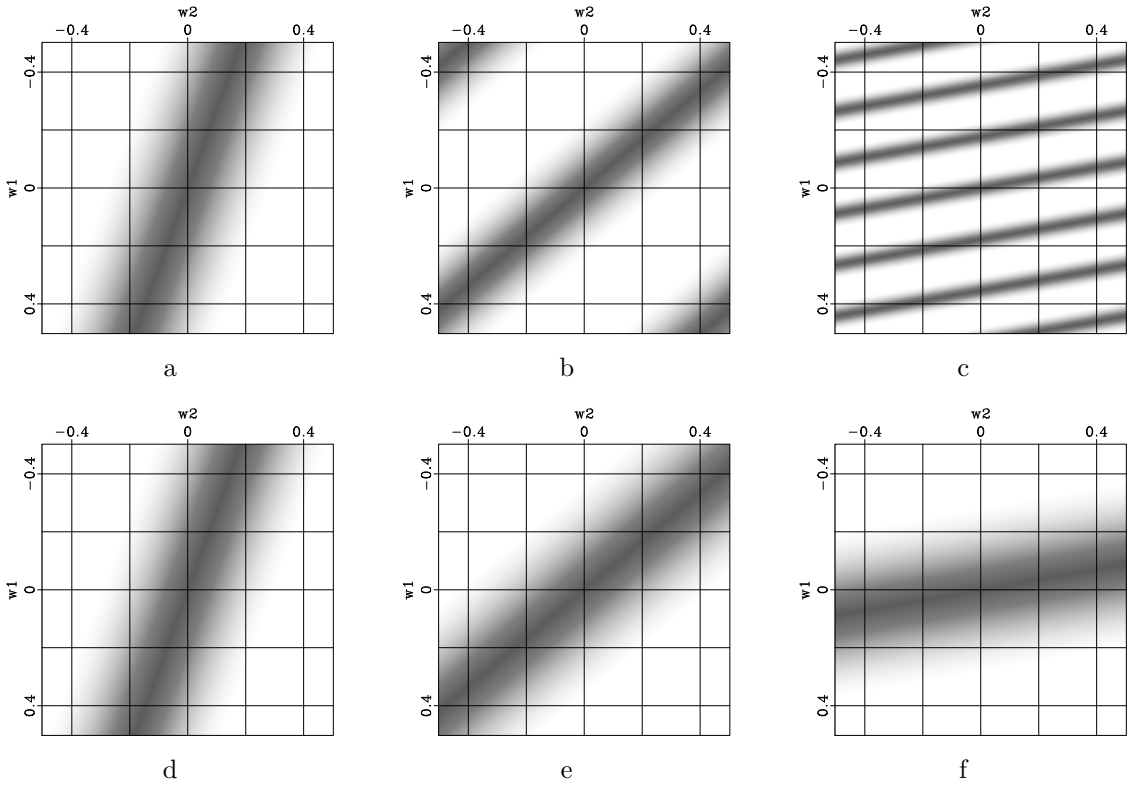

Figure 2: Magnitude responses of the line-interpolating PWD $1 - Z_1 Z_2^p$ (top) and the circle-interpolating PWD $1 - Z_1^{p_1} Z_2^{p_2}$ with $r = 1$ (bottom): from left to right $\theta = 20°, 50°, 80°$. Here, $w1$ and $w2$ are normalized frequencies (0.5 denotes Nyquist frequency, half the sampling frequency) in vertical and horizontal directions. White color denotes one and dark denotes zero.

become slightly aliased (Figure 2b), while the circle-interpolating PWD is not aliased (Figure 2e); as θ increases to 80°, the former is badly aliased (Figure 2c), and the latter is still not aliased (Figure 2f).

In summary, the line-interpolating PWD has different frequency responses for different dip angles. It may become aliased when the slope is large. The circle-interpolating PWD avoids aliasing for both small and large dip angles.

In line-interpolating PWD, we must design a digital filter to approximate the linear phase operator (or phase shift operator) Z_1^p. The slope has an infinite range $[-\infty, +\infty]$. In circle-interpolating PWD, there are two linear phase operators $Z_1^{p_1}$ and $Z_2^{p_2}$, related to the respective directions. Both the slopes p_1, p_2 have a finite range $[-r, r]$.

Following Fomel (2002), the phase shift operators can be approximated by the following maxflat fractional delay filter (Thiran, 1971):

$$H_1(Z_1) = \frac{B(1/Z_1)}{B(Z_1)} \approx Z_1^p, \tag{3}$$

where

$$B(Z_1) = \sum_{k_1=-N}^{N} b_{k_1} Z_1^{-k_1}, \tag{4}$$

N is the filter order and coefficients b_{k_1} are polynomial functions of local slopes p (Chen et al., 2013):

$$b_{k_1}(p) = \frac{(2N)!(2N)!}{(4N)!(N+k_1)!(N-k_1)!} \prod_{m=0}^{N-1-k_1} (m - 2N + p) \prod_{m=0}^{N-1+k_1} (m - 2N - p). \tag{5}$$

In Figure 3, we show the phase approximating performances of the maxflat fractional delay filters for different slopes. For small slope $p = 0.2$, the approximations are good, but when the slopes become large, the phases get wrapped. It is obvious that the phase wrapping comes when and only when $p > 1$. The larger the slope p, the more narrow the linear-phase frequency bands become.

As mentioned above, in line-interpolating PWC, the slope p is in the infinite interval $[-\infty, +\infty]$. For steep structures, where the slope p becomes larger than 1, there may be phase wrapping in the linear phase approximator. However, in circle-interpolating PWC, the ranges of p_1, p_2 can be easily controlled by the radius r. If we choose $r \leq 1$, the circle-interpolating can avoid phase wrapping completely for all dip angles.

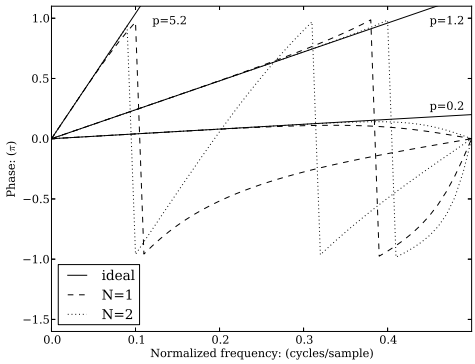

Figure 3: Phase approximating performances of the maxflat fractional delay filter $H_1(Z_1)$ when $p = 0.2, 1.2, 5.2$: dash lines denote first-order filter and dotted lines denote second-order filter.

2D LINEAR PHASE APPROXIMATION

Similar to the line-interpolating PWD, the 2D phase shift operator $Z_1^{p_1}Z_2^{p_2}$ can be approximated by the following 2D allpass system:

$$H_2(Z_1,Z_2)=\frac{F(1/Z_1,1/Z_2)}{F(Z_1,Z_2)}, \tag{6}$$

where

$$F(Z_1,Z_2)=\sum_{k_1=-N}^{N}\sum_{k_2=-N}^{N} f_{k_1k_2}Z_1^{-k_1}Z_2^{-k_2}. \tag{7}$$

2D maxflat condition

The frequency response of the objective phase shift operator is $Z_1^{p_1}Z_2^{p_2}=e^{\mathrm{j}(w_1p_1+w_2p_2)}$, where, w_1,w_2 are frequencies in radius in vertical and horizontal directions. We must design the coefficients $f_{k_1k_2}$ so that the allpass system $H_2(Z_1,Z_2)$ can obtain a similar linear phase response. The frequency response of $H_2(Z_1,Z_2)$ is

$$H_2(e^{\mathrm{j}w_1},e^{\mathrm{j}w_2})=\frac{F^*(e^{\mathrm{j}w_1},e^{\mathrm{j}w_2})}{F(e^{\mathrm{j}w_1},e^{\mathrm{j}w_2})}=e^{-\mathrm{j}2\theta_F(w_1,w_2)}, \tag{8}$$

where $\theta_F(w_1,w_2)$ is the phase of $F(Z_1,Z_2)$, which takes the following form:

$$\theta_F(w_1,w_2)=-\tan^{-1}\frac{\sum_{k_1=-N}^{N}\sum_{k_2=-N}^{N} f_{k_1k_2}\sin(k_1w_1+k_2w_2)}{\sum_{k_1=-N}^{N}\sum_{k_2=-N}^{N} f_{k_1k_2}\cos(k_1w_1+k_2w_2)}. \tag{9}$$

The phase approximating error is $w_1p_1+w_2p_2+2\theta_F(w_1,w_2)$. In order to obtain an analytical $f_{k_1k_2}$, we remove $\tan^{-1}$ and redefine the phase approximating error as

$$\begin{aligned}\epsilon(w_1,w_2) &= \tan(\frac{w_1p_1+w_2p_2}{2})-\frac{\sum_{k_1=-N}^{N}\sum_{k_2=-N}^{N} f_{k_1k_2}\sin(k_1w_1+k_2w_2)}{\sum_{k_1=-N}^{N}\sum_{k_2=-N}^{N} f_{k_1k_2}\cos(k_1w_1+k_2w_2)}\\ &= \frac{\sum_{k_1=-N}^{N}\sum_{k_2=-N}^{N} f_{k_1k_2}\sin[w_1(\frac{p_1}{2}-k_1)+w_2(\frac{p_2}{2}-k_2)]}{\cos(\frac{w_1p_1+w_2p_2}{2})\sum_{k_1=-N}^{N}\sum_{k_2=-N}^{N} f_{k_1k_2}\cos(k_1w_1+k_2w_2)}.\end{aligned} \tag{10}$$

The sine function in the numerator can be expressed by 2D Taylor's expansion as

$$\begin{aligned}&\sin(w_1(\frac{p_1}{2}-k_1)+w_2(\frac{p_2}{2}-k_2))\\ =\;&\sum_{j_1=0}^{\infty}\sum_{j_2=0}^{\infty}(-1)^{j_1+j_2}\frac{(\frac{p_1}{2}-k_1)^{2j_1+1}(\frac{p_2}{2}-k_2)^{2j_2+1}}{(2j_1+1)!(2j_2+1)!}w_1^{2j_1+1}w_2^{2j_2+1}.\end{aligned}$$

We use the maxflat phase criterion (Thiran, 1971), which means that the filter has a phase response as flat as the desired linear response. In the 2D case, the criterion is equivalent to the mathematical expression that the partial derivatives of the error function should be as small as possible. We set them to be zero:

$$\frac{\partial^{j_1+j_2}\epsilon(w_1,w_2)}{\partial w_1^{j_1}\partial w_2^{j_2}}=0 \qquad j_1,j_2=0,1,\dots\ , \tag{11}$$

which is equivalent to the following 2D maxflat condition:

$$\sum_{k_1=-N}^{N}\sum_{k_2=-N}^{N}(\frac{p_1}{2}-k_1)^{2j_1+1}(\frac{p_2}{2}-k_2)^{2j_2+1}f_{k_1k_2}=0. \tag{12}$$

Additional constraint

The above maxflat condition is a linear system with $(2N+1)^2$ unknown variables $f_{k_1k_2}$. In order to obtain a non-zero solution, we use only the first $4N^2+4N$ equations, which zeros the partial derivatives with order less than $(2N+1)^2$, and impose an additional constraint on the filter coefficients,

$$\sum_{k_1=-N}^{N}\sum_{k_2=-N}^{N}f_{k_1k_2}=1. \tag{13}$$

This additional constraint yields a unit amplitude response at zero frequency, similarly to the 1D maxflat approximation (Chen et al., 2013).

Directional separability

The combined linear system can be solved analytically. It is based on the property that $f_{k_1k_2}$ can be decoupled into the product of two terms, as shown in the appendix,

$$f_{k_1k_2}(p_1,p_2)=b_{k_1}(p_1)b_{k_2}(p_2), \tag{14}$$

where $b_{k_1}(p_1)$ and $b_{k_2}(p_2)$ denote coefficients of the 1D maxflat fractional delay filter used to approximate $Z_1^{p_1}$ and $Z_2^{p_2}$ respectively. Equation 14 implies that the 2D maxflat filter $H_2(Z_1,Z_2)$ is equivalent to a cascade of two 1D maxflat filters,

$$H_2(Z_1,Z_2)=\frac{B_1(1/Z_1)}{B_1(Z_1)}\frac{B_2(1/Z_2)}{B_2(Z_2)}. \tag{15}$$

$B_1(Z_1)$ and $B_2(Z_2)$ can be designed in the same way as for the line-interpolating PWD, whose coefficients are given by equation 5. $H_2(Z_1, Z_2)$ can be implemented by applying the 1D maxflat filter on each direction independently.

This separability of the maxflat linear phase filter extends to 3D and higher dimensions.

Frequency responses

We show the magnitude responses of the infinite impulse response (IIR) omnidirectional PWD (OPWD) $1 - H_2(Z_1, Z_2)$ when $N = 2$ in Figure 4d-f. Compared with the ideal responses in Figure 2, it has good approximations for all the three dip angles in most of the frequency band. There are distortions in the high frequency bands, due to phase approximation errors in $H_2(Z_1, Z_2)$ for high frequencies. They are not significant in practice, because the frequency band of seismic data is temporally limited.

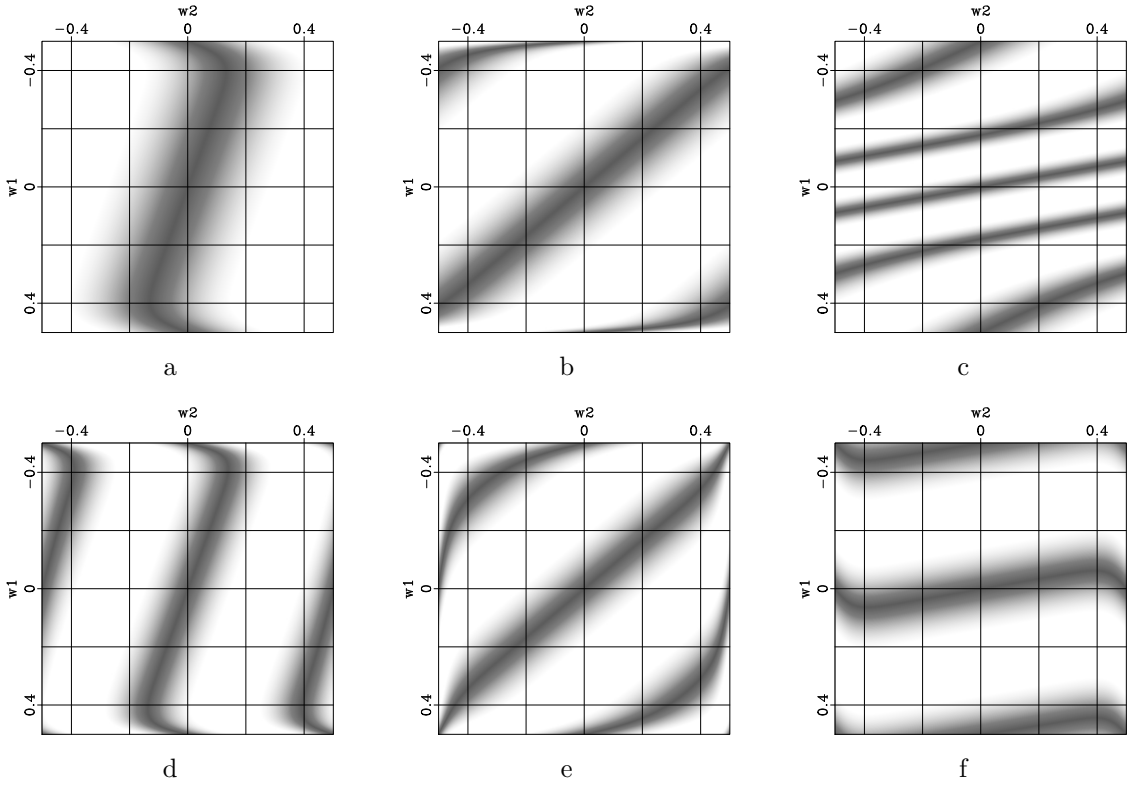

Figure 4: Magnitude responses of the IIR implementation of LPWD $1 - Z_2 H_1(Z_1)$ (top) and OPWD $1 - H_2(Z_1, Z_2)$ (bottom): from left to right $\theta = 20°, 50°, 80°$.

When $\theta = 20°$ or $50°$, the omnidirectional PWD has a low-frequency response similar to that of line-interpolating PWD (LPWD) shown in Figure 4a-b. When $\theta = 80°$, the LPWD has aliasing in low-frequency bands (Figure 4c), while the OPWD exhibits a more desirable low-frequency response (Figure 4f).

Following Fomel (2002), the IIR LPWD $1 - Z_2 H_1(Z_1)$ can be approximated by the following finite impulse response (FIR) filter:

$$H_3(Z_1, Z_2) = B(Z_1) - Z_2 B(1/Z_1). \tag{16}$$

Similarly, the IIR OPWD filter $1 - H_2(Z_1, Z_2)$ can also be approximated by an FIR implementation:

$$H_4(Z_1, Z_2) = F(Z_1, Z_2) - F(1/Z_1, 1/Z_2). \tag{17}$$

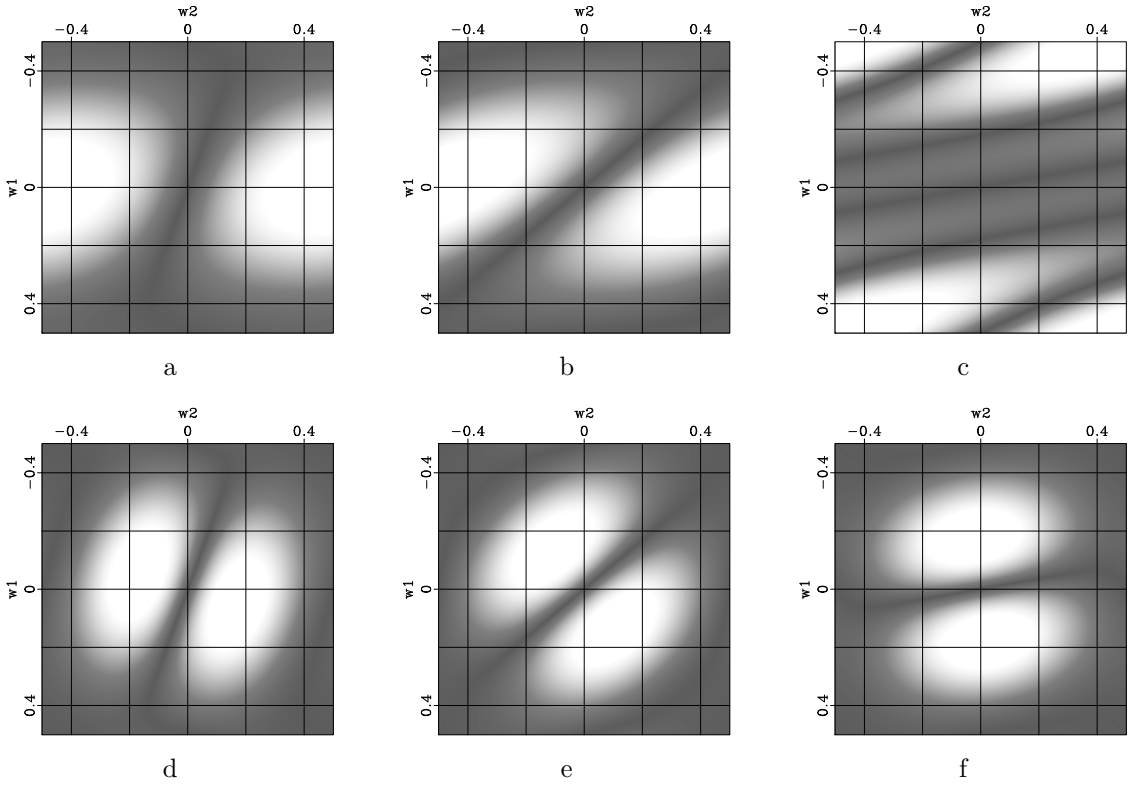

Figure 5: Magnitude response of the FIR approximation of LPWD $H_3(Z_1, Z_2)$ (top) and OPWD $H_4(Z_1, Z_2)$ (bottom): from left to right $\theta = 20°, 50°, 80°$.

The frequency responses of these two FIR approximations are shown in Figure 5. Similar to the IIR implementation, the FIR OPWD (Figure 5d-f) can obtain an expected low-frequency response for all three dip angles. While the FIR LPWD cannot obtain a good low-frequency response when $\theta = 80°$ (Figure 5c). Compared with the IIR implementations, the FIR approximations of both LPWD and OPWD have less desirable high-frequency responses.

APPLICATIONS

Omnidirectional dip estimation

Dip estimation by OPWD is equivalent to the parameter estimation of the OPWD filter in equation 17. The desired parameters p_1, p_2 minimize the predictive error:

$$H_4(Z_1, Z_2, p_1, p_2)U \approx 0, \tag{18}$$

with

$$p_1^2 + p_2^2 = r^2. \tag{19}$$

We solve the above equation set by Newton's search. At each iteration, the increments $\Delta p_1, \Delta p_2$ are calculated from the following linearization:

$$\begin{bmatrix} \frac{\partial H_4}{\partial p_1}U & \frac{\partial H_4}{\partial p_2}U \\ 2p_1 & 2p_2 \end{bmatrix} \begin{bmatrix} \Delta p_1 \\ \Delta p_2 \end{bmatrix} \approx \begin{bmatrix} -H_4U \\ r^2 - p_1^2 - p_2^2 \end{bmatrix}. \tag{20}$$

Both p_1 and p_2 are updated until the residual of OPWD becomes less than a specified tolerance. Similarly to the line-interpolating PWD, when we are solving for Δp_1 and Δp_2, either Tikhonov's regularization (Fomel, 2002) or shaping regularization (Fomel, 2007) can be applied to obtain a robust estimation.

In order to test the performance of OPWD, we generate a 2D synthetic image in polar coordinates using the following equation:

$$u(r) = e^{-\alpha r}\sin(2\pi(f_0 + \beta r)r). \tag{21}$$

Structures in this image have constant dip angles along radial directions, but the frequency and magnitude vary with radius. Figure 6a shows a test example with $f_0 = 0.02$, $\alpha = 0.01, \beta = 0.0005$. We apply the first-order ($N = 1$) OPWD filter to this test image. With the starting dip $\theta_0 = \frac{\pi}{4}$, we obtain an estimation result in 10 iterations, as shown in Figure 6b. Obviously, dip estimation by OPWD is effective for both horizontal and vertical structures.

We compare the proposed OPWD with LPWD by estimating errors in Figures 6c and 6d. As the test image is noise-free, we do not need to use any smoothing regularization in both of these methods. In this case, the modeling errors are the dominate factor of the final estimating errors. Obviously, the LPWD cannot detect the vertical structure accurately, while the OPWD can.

Improved predictive picking

Event picking is a useful tool for interpretation. However, when there are salt bodies and buried hills in our images, picking becomes difficult. Using some additional

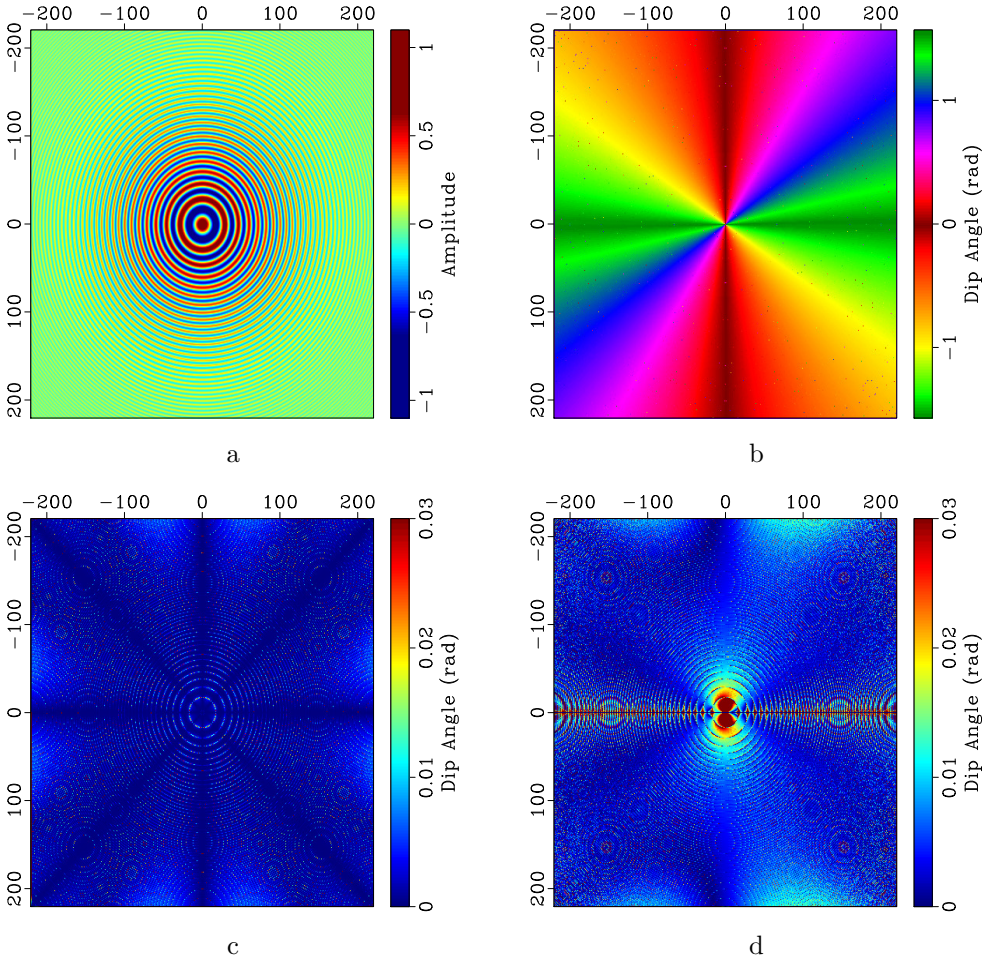

Figure 6: An omnidirectional dip estimation example: (a) test image; (b) dip angles estimated by the OPWD filter; (c) estimation error of OPWD; (d) estimation error of LPWD.

information, such as cross-correlation analysis (Yung and Ikelle, 1997), high-order statistics (Srinivasan and Ikelle, 2001) or local slope fields (Fomel, 2010), automatic picking tools can be improved. A challenge for automatic picking is therefore the robust estimation of the statistics or slope fields. This challenge is especially difficult near boundaries of salt bodies and buried hills because of steep structures. In this paper, we use the slope-based predictive painting method (Fomel, 2010) to pick events. We use the proposed OPWD to estimate the slope field, and show how it improves event-picking results.

In Figure 7, we show a profile of a post-stack dataset from an oilfield in China. We can see a buried hill in this area, and there are several steep boundaries and faults near the buried hill. The slope field estimated by OPWD is shown in Figure 8a. Compared with the slope by LPWD in Figure 8b, the OPWD yields a larger estimated slope near the 360-th trace and the 475-th trace. As shown in Figure 7, there exist faults and steep buried-hill boundaries at these two positions, respectively. In this application, we use the shaping regularization with 25-points window size. We choose the 400-th and 560-th traces as two reference traces and use the two slope fields in 2D predictive painting. Painting results are shown in Figure 9a and Figure 9b. Meanwhile, we pick some of the events, as shown in Figure 10. Compared with the painting and picking results based on the LPWD, the OPWD provides more reasonable results near the fault (360-th trace) and near the buried-hill boundaries (475-th trace).

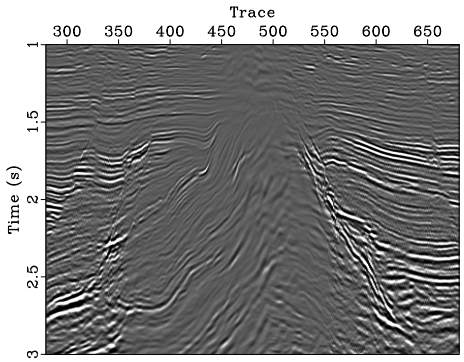

Figure 7: Field data example: steep structures and faults are rich in this selected area.

CONCLUSIONS

We have addressed the problem of steep slope estimation by introducing a novel circle-interpolating method in plane-wave construction, which leads to omnidirectional plane-wave destruction. Frequency analysis demonstrates the ability of the proposed method to handle steep structures. We presented both synthetic and field data examples to show the performance of the omnidirectional dip estimation. The

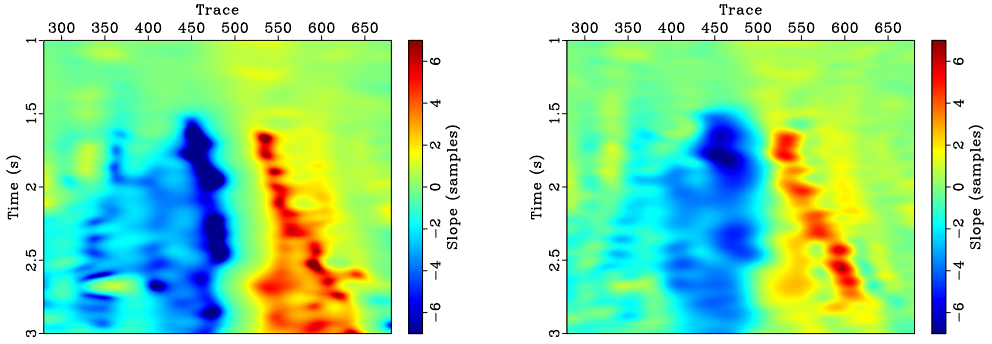

Figure 8: Slope field estimated by OPWD (a) and LPWD (b). In both the two methods, we choose $N = 2$ and use 25 points regularization window in each directions.

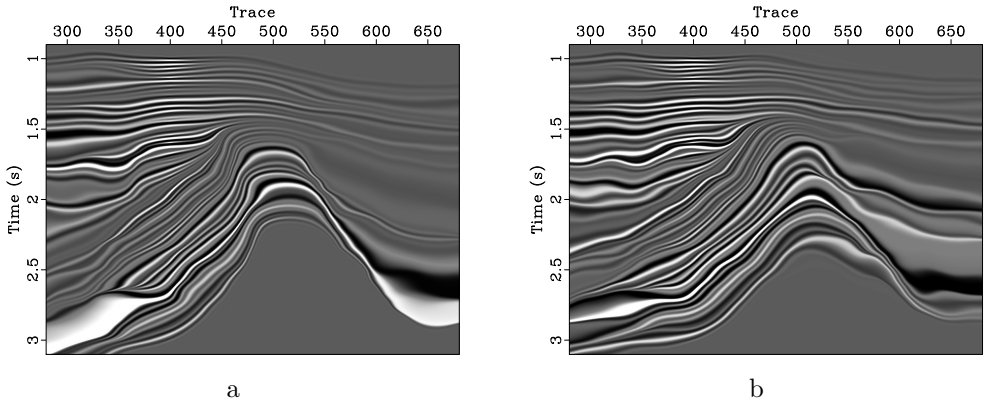

Figure 9: Predictive painting results using the OPWD slope (a) and LPWD slope (b): the reference traces are the 400-th and 560-th traces.

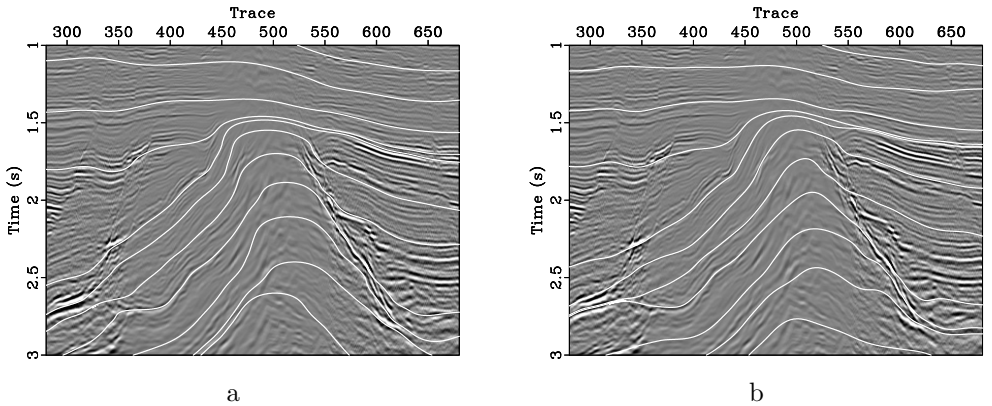

Figure 10: Predictive picking results using the OPWD slope (a) and LPWD slope (b).

new estimation method can also be used in other applications that require slope fields for steep structures, such as attribute analysis on a migrated image or a time slice.

As a byproduct, we proved that the high-dimensional maxflat fractional delay filter is separable in all directions. A typical $m-$dimensional $n-$th order ($n = 2N + 1$ in this paper) linear-phase approximating system is supported by n^m coefficients. Using the separability property, the maxflat linear-phase approximating system has only mn coefficients. It is useful in applications that require high-dimensional linear-phase approximations.

ACKNOWLEDGMENT

The joint research is sponsored by by China Scholarship Council and China State Key Science and Technology Projects (2011ZX05023-005-007). We thank the reviewers and the Associate Editor for their helpful suggestions.

APPENDIX: SEPARABILITY OF THE 2D MAXFLAT FILTER

Following Thiran (1971), the maxflat condition of 1D fractional delay filter $B_1(1/Z_1)/B_1(Z_1)$ is expressed as

$$\sum_{k_1=-N}^{N} (\frac{p_1}{2} - k_1)^{2j_1+1} b_{k_1}(p_1) = 0 \ , \qquad j_1 = 0, \ldots, 2N-1. \tag{A-1}$$

With the additional constraint (Chen et al., 2013)

$$\sum_{k_1=-N}^{N} b_{k_1}(p_1) = 1, \tag{A-2}$$

we can obtain the unique $b_{k_1}(p_1)$. Similarly, $b_{k_2}(p_2)$ satisfies the following linear system:

$$\begin{cases} \displaystyle\sum_{k_2=-N}^{N} (\frac{p_2}{2} - k_2)^{2j_2+1} b_{k_2}(p_2) = 0 \ , \quad j_2 = 0, \ldots, 2N-1 \\ \displaystyle\sum_{k_2=-N}^{N} b_{k_2}(p_2) = 1 \end{cases} . \tag{A-3}$$

Substituting $b_{k_1}(p_1)b_{k_2}(p_2)$ into the 2D maxflat equation 12, for all $j_1, j_2 = 0, \ldots, 2N-1$, we obtain

$$\sum_{k_1=-N}^{N} (\frac{p_1}{2} - k_1)^{2j_1+1} b_{k_1}(p_1) \sum_{k_2=-N}^{N} (\frac{p_2}{2} - k_2)^{2j_2+1} b_{k_2}(p_2) = 0. \tag{A-4}$$

Also, for $j_1 = 2N$, and $j_2 = 0, \ldots, 2N-1$ or $j_2 = 2N$, and $j_1 = 0, \ldots, 2N-1$, equation 12 still holds true.

Substituting $b_{k_1}(p_1)b_{k_2}(p_2)$ into the additional constraint in Equation 13,

$$\sum_{k_1=-N}^{N} b_{k_1}(p_1) \sum_{k_2=-N}^{N} b_{k_2}(p_2) = 1. \tag{A-5}$$

In other words, $b_{k_1}(p_1)b_{k_2}(p_2)$ is a solution of the combined linear system of equation 12 and 13. This linear system must have a unique solution, therefore

$$f_{k_1 k_2}(p_1, p_2) = b_{k_1}(p_1)b_{k_2}(p_2). \tag{A-6}$$

REFERENCES

Bardan, V., 1987, Trace interpolation in seismic data processing: Geophysical Prospecting, **35**, 343–358.

Barnes, A. E., 1996, Theory of 2-D complex seismic trace analysis: Geophysics, **61**, 264–272.

Chen, Z., S. Fomel, and W. Lu, 2013, Accelerated plane-wave destruction: Geophysics, **78**, V1–V9.

Claerbout, J. F., 1992, Earth soundings analysis: Processing versus inversion: Blackwell Scientific Publications.

Davis, S., 1991, Low-dispersion finite difference methods for acoustic waves in a pipe: The Journal of the Acoustical Society of America, **90**, 2775–2781.

Fomel, S., 2002, Applications of plane-wave destruction filters: Geophysics, **67**, 1946–1960.

———, 2007, Shaping regularization in geophysical-estimation problems: Geophysics, **72**, R29–R36.

———, 2010, Predictive painting of 3D seismic volumes: Geophysics, **75**, A25–A30.

Fomel, S., and A. Guitton, 2006, Regularizing seismic inverse problems by model reparameterization using plane-wave construction: Geophysics, **71**, A43–A47.

Fomel, S., E. Landa, and M. T. Taner, 2007, Poststack velocity analysis by separation and imaging of seismic diffractions: Geophysics, **72**, U89–U94.

Hale, D., 2007, Local dip filtering with directional Laplacians: CWP Report, **567**.

Harlan, W. S., J. F. Claerbout, and F. Rocca, 1984, Signal/noise separation and velocity estimation: Geophysics, **49**, 1869–1880.

Marfurt, K. J., 2006, Robust estimates of 3D reflector dip and azimuth: Geophysics, **71**, P29–P40.

Marfurt, K. J., V. Sudhaker, A. Gersztenkorn, K. D. Crawford, and S. E. Nissen, 1999, Coherency calculations in the presence of structural dip: Geophysics, **64**, 104–111.

Noye, B., 2000, Explicit finite difference methods for variable velocity advection in the presence of a source: Computers & Fluids, **29**, 385 – 399.

Schleicher, J., J. C. Costa, L. T. Santos, A. Novais, and M. Tygel, 2009, On the estimation of local slopes: Geophysics, **74**, P25–P33.

Srinivasan, K., and L. T. Ikelle, 2001, Short note: Applications of third-order statistics for the automatic time picking of seismic events: Geophysical Prospecting, **49**, 155–158.

Thiran, J., 1971, Recursive digital filters with maximally flat group delay: IEEE Transactions on Circuit Theory, **18**, 659–664.

Yung, S. K., and L. T. Ikelle, 1997, An example of seismic time picking by third-order bicoherence: Geophysics, **62**, 1947–1952.

Zhang, X., 2009, Maxflat fractional delay IIR filter design: IEEE Transactions on Signal Processing, **57**, 2950 –2956.